Journal of Materials Chemistry A

ROYAL SOCIETY OF CHEMISTRY

PAPER

View Article Online
View Journal | View Issue



Cite this: J. Mater. Chem. A, 2024, 12, 30442

# Tuneable and efficient manufacturing of Li-ion battery separators using photopolymerization-induced phase separation†

Samuel Emilsson, [a] Göran Lindbergh [b] and Mats Johansson *[a]

In an effort to increase the thermomechanical stability of lithium-ion battery separators, thermoset membranes (TMs) are a viable alternative to commercial polyolefin separators. We present an efficient and scalable method to produce thin TMs *via* photopolymerization-induced phase separation (PIPS) in ambient conditions. The pore size is controllable and tuneable by varying the ratio between propylene carbonate (PC) and tetraethylene glycol (TEG) as porogens. The TMs maintain dimensional stability above 200 °C and display sufficient mechanical stiffness. By incorporating a small amount of a thiol monomer, the brittleness of the TMs was suppressed, and a high Young's modulus was achieved (880 MPa). The ionic conductivity of the optimized TMs was around 1 mS $cm^{-2}$, with a low MacMullin number, $N_M$ (4.9). In symmetrical Li/Li cells, the TMs behaved similarly to the commercial PE reference, effectively suppressing short circuits for 1000+ hours although continuous overpotential build-up and electrolyte consumption eventually led to cell failure. In $LiFePO_4$/Li half-cells, similar rate capabilities were achieved for the TMs compared to the reference showing its viability as a separator material.

Received 28th May 2024
Accepted 10th October 2024

DOI: 10.1039/d4ta03701d

rsc.li/materials-a



## 1. Introduction

To meet the ambitious climate goals set up by the UN Paris Climate Accords, decarbonisation through electrification plays a key role. For this, the demand for batteries is expected to grow rapidly, with the automotive industry leading the way. This rapid expansion of the automotive industry puts heightened demands on batteries which should have high energy density, but also increased safety and longevity.[1] Furthermore, the production of these batteries should be done in a sustainable and affordable way, at large scale. This puts rather heavy constraints on new battery materials development, where these factors should be considered.

An often-overlooked aspect of materials development for batteries is the separator. The main purpose of the separator is to prevent electrical and physical contact between the electrodes while its porous structure allows an electrolyte (typically liquid) to transport ions. Conventionally, the separator is therefore a passive component. Despite this, it plays a vital role in the safety and performance of the battery. A separator should have low ionic resistance, high wettability, good mechanical and thermal stability.[2,3] In this study we aim to develop a novel type of separator based on a thermoset polymer that meets these requirements, and can also be produced easily at scale.

The current state-of-the-art are microporous thermoplastic polyolefin separators (either polyethylene (PE) or polypropylene (PP) based). They are produced at large scale at a reasonable cost and display several advantages such as low thickness (≈20 μm) and high chemical and mechanical stability. However, they typically suffer from poor wettability and thermal stability due to their moderate melting point (<170 °C).[4] To counteract this safety issue, tri-layer PP/PE/PP separators have been developed with a shutdown mechanism *i.e.* the middle PE layer melts first and closes the pores. However, this tri-layer setup leads to a decrease in power capabilities. In addition, the polyolefin separators that are power optimized (high ionic conductivity) have lower mechanical properties, meaning a compromise is typically made between these different properties.

A variety of alternative separator technologies have been reported in the literature.[3,5,6] Firstly, multiple surface treatment strategies have been developed to increase electrolyte wettability and thermal stability of polyolefin separators, which has also been implemented industrially.[5] Several ceramic coatings (such as aluminum oxide) have been employed, leading to lower thermal shrinkage at 150 °C and a higher affinity to the liquid electrolyte, boosting the ionic conductivity.[5,7,8] High energy radiation-induced oxidation is also a technique that has been used to improve the surface properties of the separators.[9] Several nonwoven membrane materials have also been explored. Cellulose-based separators can exhibit excellent ionic conductivities and thermal stability, but a challenge has been to

[a]Division of Coating Technology, Department of Fibre and Polymer Technology, KTH Royal Institute of Technology, SE-100 44 Stockholm, Sweden. E-mail: matskg@kth.se
[b]Division of Applied Electrochemistry, Department of Chemical Engineering, KTH Royal Institute of Technology, SE-100 44 Stockholm, Sweden

† Electronic supplementary information (ESI) available. See DOI: https://doi.org/10.1039/d4ta03701d

control porosity for longer-term cycling stability in a scalable way.[10] In addition, a multitude of separators developed *via* electrospinning (such as PET, PAN and PI) have been explored.[5]

Novel separators have also shown the possibility to enhance the performance of next generation batteries.[11] For instance, by increasing cycle life of Li-metal batteries by suppressing lithium dendrite growth.[12,13] A limitation with these studies is the use of traditional liquid electrolytes that ultimately degrade over time and where safety is still of concern. However, separators can also play a role as mechanical support in soft polymer or gel electrolytes, since thin separators can be achieved while still maintaining mechanical stability. Therefore, several studies have infused polymer electrolytes into separators, displaying better stability.[14–17] For these applications, the dimensional stability at high temperatures increases in importance, allowing for safe high temperature operation.

A crucial aspect in the development of novel separator materials, is the scalability of their production. For polyolefin separators, two production pathways have been established, dry and wet processing. In wet processing, plasticizers are added to PE and films are biaxially stretched. Solvents are then used to remove the plasticizers, and the films are dried. Dry processing involves extruding polyolefin melts, annealing and uniaxially stretching. Celgard's PP and trilayer PP/PE/PP separators (often used in literature) are made this way.[18] This method is attractive from a cost and environmental standpoint, since it doesn't require solvents. Despite this, wet processing makes up a majority of the market share thanks to the versatility of the process. In addition to this, both the wet and dry processes may require additional surface treatment steps to increase wettability and thermal stability.[18,19] Therefore, developing novel methods for separator production that are versatile but still efficient and sustainable is highly attractive.

Bicontinuous polymer monoliths formed *via* polymerization-induced phase separation (PIPS) are a promising alternative. First developed for separation media, the principle behind PIPS involves the mixture of monomers with porogenic solvents that, when polymerized, phase separate to form a porous structure.[20–22] By tuning the monomer(s) and porogenic solvent(s) structure and content, a wide variety of morphologies and porosities can be achieved.[23,24] In addition, the resin mixture can be filled or infused into molds to achieve porous monoliths in a wide variety of geometries. By using crosslinking monomers, porous thermosets are obtained, which are known for their high chemical and thermal stabilities.[25]

In the context of batteries, several electrolyte systems have been developed using PIPS. Schulze *et al.* used PIPS to form polymer electrolytes with a structural phase and an ion-conducting phase.[26] PIPS has also proven useful for creating electrolytes with good mechanical properties for structural power applications.[27,28] Shirshova *et al.* has used it to form a structural supercapacitor electrolyte with a porous epoxy phase and an ionic liquid phase.[29,30] In our research group, structural battery electrolytes have been developed by combining a dimethacrylate monomer with carbonate solvents, forming a high modulus electrolyte that has been used in structural batteries.[31–36]

PIPS has also been used in developing new separator materials. Sakakibara *et al.* developed an epoxy-based separator using low molecular poly(ethylene oxide) as a porogen.[37] The pore size was also engineered by introducing a block copolymer surfactant. Li *et al.* used a similar system, but introduced ceramic particles (LLTO) into the structure to increase ionic transport properties.[13] Recently, Manly *et al.* used UV-induced PIPS to form acrylate-based separators with ethylene carbonate (EC) as a porogen which could be used in a battery without washing away any solvent, but thereby requires production in inert conditions.[38,39]

In the present study, UV-induced PIPS is used to create methacrylate-based thermoset membranes (TM). A scalable process was developed in which UV-curing can be used in a continuous fashion at ambient conditions. In a first investigation, a combination of tetraethylene glycol (TEG) and propylene carbonate (PC) as cheap and recyclable porogens were used. By using different combinations of these porogens, a simple way of tuning the morphology of the TMs is shown. The TMs also display high thermomechanical stability, with a dimensional stability above 200 °C. In a second optimization, the addition of a small amount of a thiol monomer is presented to increase processability of the TMs. The toughness of the TMs increased significantly, making it possible to produce thin membranes (<30 μm). The TMs are compared to a commercial PE separator, displaying similar cycling performance in symmetrical Li/Li cells and towards commercial electrodes.

## 2. Experimental

### 2.1. Materials

Bisphenol A ethoxylate dimethacrylate ($M_n$ = 540 g mol$^{-1}$) was provided by Sartomer Company, Europe. Tris(2-(3-mercaptopropionyloxy)ethyl)isocyanurate (TEMPIC) was provided by Bruno Bock GmbH. Irgacure 651 (2,2-dimethoxy-1,2-diphenylethan-1-one) was purchased from BASF. Tetra(ethylene glycol) (99%) was purchased from Aldrich. Poly(vinyl alcohol) (PVA) (99+% hydrolyzed), propylene carbonate (PC) (99.7%) was purchased from Sigma-Aldrich. Battery grade 1 M lithium hexafluorophosphate ($LiPF_6$) in ethylene carbonate (EC) : diethyl carbonate (DEC) (1 : 1 v/v) and lithium ribbons (99.9%, 0.75 mm thick) were purchased by Sigma-Aldrich. A commercial PE separator was used as reference material.

### 2.2. Membrane fabrication procedure

Prior to the fabrication, glass plates were coated with poly(vinyl alcohol) (PVA) solution. A PVA solution was prepared by dissolving 1 wt% PVA in deionized water for 2 hours at 90 °C. The glass was oxygen plasma treated for 2 minutes to increase wettability and an applicator was used to apply a thin layer (50 μm) of the PVA solution. The glass plates were then dried at 120 °C for 1 h.

A precursor resin mixture was made by combining a fixed ratio of tetraethylene glycol (TEG) and propylene carbonate (PC) with the monomer bisphenol A ethoxylate dimethacrylate (BMA, $M_n$ = 540 g mol$^{-1}$) and the photo initiator Irgacure 651 (0.1 wt%

Table 1 Chemical compositions (w/w) of the thermoset membranes synthesized in the study for full characterization[a]

| Sample | TEG | PC | BMA | TEMPIC |
|---|---|---|---|---|
| TEGPC-1-40% | 0.2 | 0.2 | 0.6 | 0 |
| TEGPC-1-50% | 0.25 | 0.25 | 0.5 | 0 |
| TEGPC-2-40% | 0.27 | 0.13 | 0.6 | 0 |
| TEGPC-2-50% | 0.33 | 0.17 | 0.5 | 0 |
| TEGPC-4-40% | 0.32 | 0.08 | 0.6 | 0 |
| TEGPC-4-50% | 0.4 | 0.1 | 0.5 | 0 |
| TEGPC-4-40%-10T | 0.4 | 0.1 | 0.54 | 0.06 |
| TEGPC-2-50%-10T | 0.33 | 0.17 | 0.45 | 0.05 |

[a] Compositions of all formulations used in the initial screening test can be found in Table S1.

of monomer). In some cases, the thiol monomer tris(2-(3-mercaptopropionyloxy)ethyl)isocyanurate (TEMPIC) was also added. See Table 1 for the different compositions that were investigated. The mixture was sonicated to remove bubbles.

Using a syringe, a few droplets of the mixture was applied to the PVA-coated glass. Spacers were used to achieve the desired thickness (Kapton foil for the 20 μm membranes, clear tape for 50 μm membranes, and PTFE films for 100, 250 and 500 μm). A second PVA coated glass plate was added on top and the mixture, and two clamps were added to each side. The samples were cured using a FireJet FJ800 LED-UV lamp (60 W, 365 nm) for 120 seconds. Thicker films were flipped and cured for an additional 120 seconds.

The TMs were subsequently submerged in deionized water and gently detached from the glass plates. The TMs were kept in deionized water at 50 °C for 2 h followed by at least 12 h in room temperature to remove any residual solvent. Finally, the TMs were dried under vacuum for 16 h at 120 °C.

**2.2.1 Test series.** The sample names are denoted as follows: the first number represents the TEG : PC ratio in the porogen mixture. This is followed by the porogen content (wt%) in relation to the monomer(s). Finally, the last number represents the content (wt%) of thiol monomer (see Table 1).

### 2.3. Materials characterization

**2.3.1 Fourier-transform infrared spectroscopy (FTIR).** Fourier-transform infrared spectroscopy (FTIR) analysis was performed using a PerkinElmer Spectrum 100 in attenuated total reflection (ATR) mode equipped with a MKII Golden Gate ATR accessory (Specac Ltd). Both precursor formulations and TMs were studied. 16 spectra were recorded with a resolution of 4 $cm^{-1}$. The conversion of the methacrylate groups on BMA were followed by calculating the area under the peak at 1637 $cm^{-1}$, corresponding to the double bond and normalized based on the area of the carbonyl peaks.

**2.3.2 Thermal analysis.** The thermal properties of the TMs were investigated using a DSC1 from Mettler Toledo. Approximately 10 mg of the dried TMs were added to an aluminium pan. Under constant nitrogen flow (50 mL $min^{-1}$), the pans were initially cooled to 0 °C and subsequently heated to 200 °C. This was followed by an additional cooling and heating cycle. A cooling rate of 5 °C $min^{-1}$ heating rate of 10 °C $min^{-1}$. The second cooling and heating cycle was used to determine thermal transitions.

The thermal stability of the TMs was evaluated using thermogravimetric analysis (TGA) on a TGA 1 from Mettler Toledo. The TMs (10 mg) were heated from 30 to 600 °C at a heating rate of 10 °C $min^{-1}$ under nitrogen flow (50 mL $min^{-1}$).

**2.3.3 Thermomechanical analysis.** The thermomechanical properties of the TMs were tested using a DMA Q800 from TA Instruments in tension film mode using the ACS-3 cooling accessory. TMs with 0.5 mm thickness (the commercial reference had a thickness of 0.02 mm) were clamped with a 10–15 mm gap. A 0.1% oscillating strain was applied and the samples and cooled to 0 °C and held isothermally for 5 minutes before heating to 220 °C at a heat rate of 3 °C $min^{-1}$. Duplicates were made on all samples.

Uniaxial tensile tests were carried on a DMA Q800 from TA Instruments set at 25 °C. Specimens that were 20 × 4 mm were cut out from 100 μm thick TMs. Five specimens were tested for each formulation. An initial gap of 7 mm was used and a 10% $min^{-1}$ strain rate was used. The Young's modulus was calculated from the linear region up to 0.5%.

**2.3.4 Scanning electron microscope (SEM).** The microstructures of the TMs were characterized using the scanning electron microscopy (SEM). A Hitachi S-4800 equipped with a cold field-emission electron source was used. For viewing the cross-sections, the TMs were freeze-fractured by first submerging them in liquid nitrogen. All samples were coated with Pt/Pd for 15 seconds using a JFC 1300 fine coater from JEOL prior to analysis.

**2.3.5 Electrolyte uptake.** Inside an argon-filled glovebox, pieces of dried TMs were weighed and submerged in liquid electrolyte for 24 h. Afterward, excess electrolyte was removed from the surface of wet TMs with a tissue and then weighed again. Two to three measurements were performed for each formulation. The electrolyte uptake was calculated using the following formula:

$$\text{Electrolyte uptake} = \frac{m_{\text{wet}} - m_{\text{dry}}}{m_{\text{dry}}} \quad (1)$$

### 2.4. Electrochemical characterization

**2.4.1 Electrochemical impedance spectroscopy (EIS).** The ionic conductivities were determined by performing electrochemical impedance spectroscopy (EIS). A VMP3 potentiostat from Biologic was used and measurements were performed in the frequency range 1 MHz to 1 Hz with an AC amplitude of 10 mV. To measure the effective ionic conductivity through the TMs, 8 mm disks were punched out (250 μm in thickness) and dried. Inside an argon-filled glovebox, the disks were soaked in liquid electrolyte for 1 hour. The disks were then put into a Swagelok cell in-between two stainless steel blocking electrodes, one of which has an indent to allow excess liquid electrolyte to flow out (see Fig. S1†). A Teflon spacer with a thickness of 100 μm was also used around it. When measuring the effective conductivity through the reference, measurements

 

were made with 2 and 3 layers (due to the low thickness) and an average was taken, inspired by previous studies.[38,40] The ionic conductivity of the liquid electrolyte was taken using the same Swagelok cell but simply with a 100 μm Teflon spacer. The average of three measurements were taken.

**2.4.2 Li/Li symmetrical cell cycling.** Symmetrical lithium metal pouch cells were manufactured inside an argon-filled glovebox (<5 ppm $O_2$, <5 ppm $H_2O$). Li disks with a 14 mm diameter were used, and 100 μL liquid electrolyte was added to the separator/membrane. The cells were cycled inside a climate-controlled room (22 °C) using a Neware battery testing system with a current density of 0.5 mA $cm^{-2}$ for 1 h charge followed by 1 h discharge.

**2.4.3 Half-cell cycling.** Pouch cells (7 × 7 cm) with lithium iron phosphate (LFP) cathodes and a Li-metal anode were assembled inside an argon-filled glovebox (<5 ppm $O_2$, <5 ppm $H_2O$). First, Li metal ribbons were cut and polished with a wire brush.

For capacity retention tests, LFP electrodes (1 × 2.1 cm) were cut and a slightly oversized Li metal (1.2 × 2.3) was used. For the long-term cycling tests, a 16 mm disk of LFP was used, and an 18 mm disk of Li. First, the LFP electrode was placed inside the pouch, and 100 μL of liquid electrolyte (LP40) was added to wet the electrode. A separator/TM was then placed on top of the electrode (2 × 3) and an additional 100 μL of liquid electrolyte was added. Subsequently, the lithium metal was placed on top and the pouch was vacuum sealed. The LFP electrodes were purchased from Custom Cells Itzehoe GmbH and had an areal capacity of 2 mA h $cm^{-2}$, corresponding to an active mass loading of 13.3 mg $cm^{-2}$ (90% active mass).

For capacity retention tests, the cells were cycled inside a climate-controlled room (22 °C) using a Neware battery testing system in a potential range of 2.6 and 3.9 V *vs.* $Li^+$/Li. Two formation cycles at C/10 were followed by 5 cycles of C/5, C/2, and 1C followed by an additional 5 cycles at C/5. 1C corresponded to 150 mA $g^{-1}$ based on supplier specifications.

For long-term cycling, the cells were cycled using a VMP3 potentiostat from Biologic was used. Cells were cycled in the potential range of 2.6 and 3.9 V *vs.* $Li^+$/Li. Two formation cycles at C/10 were followed by cycling at C/5 for the subsequent cycles.

# 3. Results and discussion

## 3.1. Separator manufacturing

When designing the manufacturing process and formulations in this study, the scalability was of particular interest. Firstly, the choice of bisphenol A ethoxylate dimethacrylate (BPA-DMA) monomer stemmed from its combination of attractive properties, but also since it is produced at scale. The monomer has also been used for both UV and thermally-initiated PIPS previously, showing promising performance as hybrid electrolyte.[31,32] BPA-DMA contains a rigid aromatic structure which provides high mechanical rigidity, an important property when designing separators. The ethoxylate chains, provide some flexibility, which leads to the resin having a lower viscosity, making it easier to work with. In addition, the ethoxylate chains have the potential to interact with the liquid electrolyte, potentially increasing the electrolyte uptake. Finally, the use of methacrylates instead of *e.g.* acrylates stems from the higher glass transition temperature ($T_g$) typically seen for methacrylates, giving the separator a higher thermomechanical stability.[41] For polymerization-induced phase separation (PIPS) the choice of porogen(s) are key for the pore structures that can be obtained. Tetra(ethylene glycol) (TEG) has previously shown to form large pore morphologies when combined with epoxy systems.[37] Propylene carbonate (PC) has also been used, but generally leading to smaller pore size.[29] Thereby, a combination of these porogens were used to tune the morphology. Furthermore, both TEG and PC are considered safe and cheap solvents.[42,43] The high boiling points (240 °C for PC and 314 °C for TEG) also makes recovery of the solvents by distillation of the water during the washing process feasible.[42,43] UV-curing is also a scalable method which is suitable for manufacturing of films and coatings in a continuous process.[44]

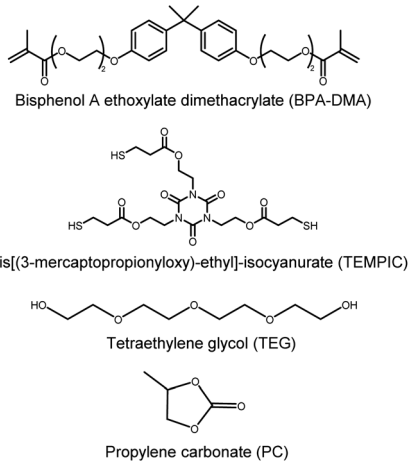


Fig. 1 Molecular structures of monomers and porogens used in the present study.

Fig. 2 shows a process schematic. An initial mixture of monomer, initiator and porogens is spread and sandwiched between two glass plates with a spacer to control the thickness. To ensure membranes with porous interfaces, a PVA layer was coated onto the glass. This strategy was previously used by Sakakibara *et al.* when making membranes from an epoxy resin combined with polyethylene glycol 200 (PEG200), where the polar hydroxyl groups on PVA was proposed to attract PEG200 to the surface.[37] They noted that when membranes were made

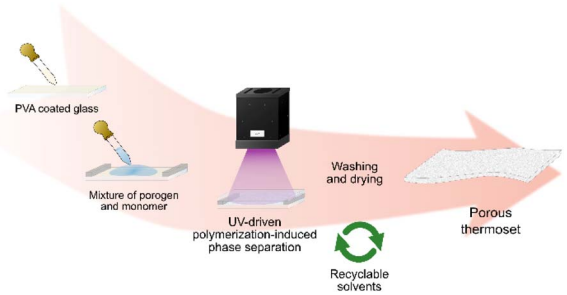


Fig. 2 Process schematic of thermoset membrane fabrication.

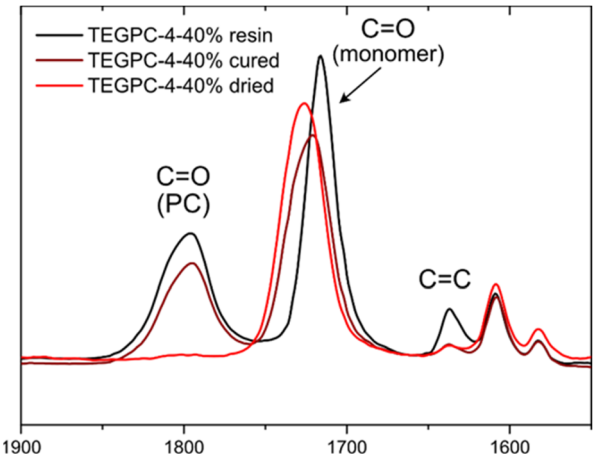


Fig. 3 FTIR spectra of TEGPC-4-40% before and after curing, and after washing and drying the membrane. The peak at 1637 $cm^{-1}$ represents the vinyl stretching mode. The peak at 1800 $cm^{-1}$ represents the carbonyl stretching on PC.

without coating the glass, a non-porous skin was obtained. Interestingly, despite both changing polymer system (from epoxy to methacrylate) and curing method (from thermal to UV-curing), a similar non-porous skin was obtained for our system as well (see Fig. S2†). Previous work on UV-driven PIPS has also suggested asymmetric porosity when comparing the top and bottom of the film.[45] For this study, symmetrical porosity was observed when using PVA-coated glass as substrates.

The resin mixtures were rapidly cured (2 × 120 s) at ambient conditions. An opaque film was obtained, implying that a phase separation had occurred. Fig. 3 shows the FTIR spectra of one formulation, TEGPC-4-40%, before and after curing. A clear reduction of the vinyl stretching mode at 1637 $cm^{-1}$ between the resin and cured film can be seen. A monomer conversion of ~80% was calculated, similar to a previous study when using the same monomer.[32] The limited conversion is likely due to vitrification occurring, due to the high $T_g$ of the dimethacrylate, lying far above the curing temperature. Unreacted monomer could potentially affect the electrochemical stability of the separator, and therefore a high conversion is preferred. However, since each monomer contains two methacrylate groups, it is likely that a majority of the remaining unreacted groups (~20%) are on partially reacted pendant monomers rather than free monomers.[46,47] After curing, the membranes detached from the glass plates in water and the porogens could be washed away. After drying under vacuum, uniformly porous membranes of different thickness were obtained, depending on the spacer used during curing. The absence of the peak at 1800 $cm^{-1}$ related to the C=O group in PC can be seen in Fig. 3, and the disappearance of the peak at 3400 $cm^{-1}$ related to the –OH groups in TEG can be seen in Fig. S3,† showing that the washing and drying process were successful *i.e.* no porogen was trapped in closed voids.

### 3.2. Effect of porogen structure and content

A screening of various compositions was performed to see how the effect of porogen content and ratio of the respective porogens affected the morphology of the porous TMs, as seen in Fig. 4. From this, two clear trends can be observed. Firstly, when increasing the porogen content, the TMs become less transparent, indicating that they contain larger pores in a dimension that scatter light. This is an expected phenomenon, well in line with literature.[48,49] Secondly, the TMs become less transparent when increasing the concentration of TEG in the composition, indicating that larger pores are formed when using TEG as a porogen compared to PC. This suggests that TEG is a rather poor solvent for BPA-DMA compared to PC. Indeed, when mixing BPA-DMA purely with TEG, an immiscible solution was obtained already before curing. However, when combining the two solvents in different composition, a variety of morphologies could be obtained, some of which can be seen in the micrographs in Fig. 4.

At the lowest porogen content (30 wt%) and TEGPC-1-30%, a completely transparent film is obtained which suggests that no proper phase separation has occurred. When increasing the TEG content to TEGPC-4-30%, a porous film is obtained (see micrograph in Fig. S5†). However, the porosity of all these samples are too low to be of relevance as separator materials. On the other hand, the highest porogen content (60 wt%) results in brittle films which fell apart when removing them

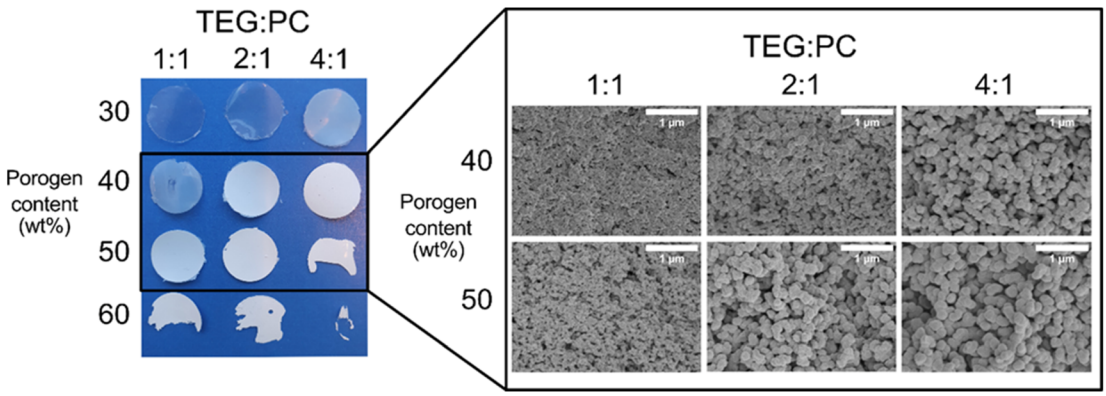


Fig. 4 (Left) Digital photographs of different porous membranes made using varying contents the porogens TEG and PC. (Right) Cross-sectional SEM micrographs of the freeze fractured films of selected formulations, showing a variation in pore size.

 

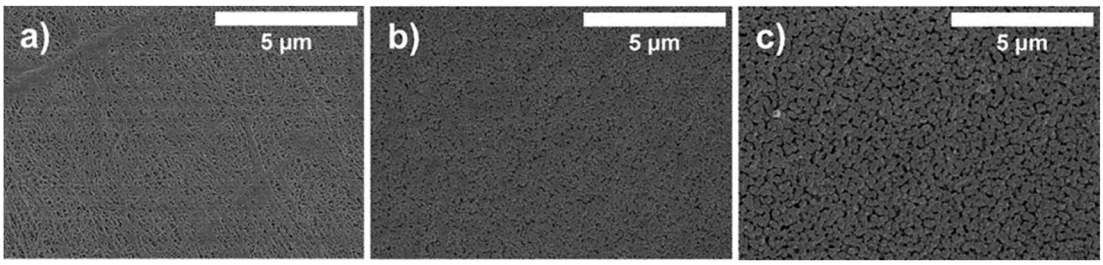


Fig. 5 Top view SEM micrographs of the surface of (a) PE reference material (b) TEGPC-2-40% and (c) TEGPC-4-40% at 10 000× magnification.

from the glass. These compositions could be useful for applications where high porosities are important, *e.g.* absorbants. Ultimately, the compositions containing 40 and 50 wt% were therefore used for further analysis as separator materials.

Although the cross-sectional micrographs seen in Fig. 4 give a good indication of the morphologies of the different compositions relative to each other, it is important to note that they are not fully representative of the true porosity. A previous study on similar systems showed that the morphology of freeze fractured samples, like the samples in this study, differed extensively from cross sectional images of samples that have been broad ion beam milled and then analysed with SEM.[35] Furthermore, as previously mentioned, the surfaces of the TMs are of vital importance to ensure good ion transport at the interfaces. Therefore, the surfaces of selected TMs were also examined (Fig. 5). The surface of TEGPC-2-40% exhibits smaller pores than TEGPC-4-40%, and both display uniformly distributed pores that are similar in scale to the commercial PE reference.

### 3.3. Thermal and mechanical properties

Apart from the morphology, the thermal and mechanical properties of the TMs are of significant importance when developing separator materials. The dimensional integrity of the separator when the temperature increases is important since it ensures that a short circuit does not occur. DSC measurements were performed to examine the thermal behaviour of one the TMs, TEGPC-4-40%, compared to a commercial PE reference. Fig. 6a shows a clear melting point at 141 °C during the heating cycle, typical for separators based on PE with a high molecular weight.[5] During the cooling cycle, a crystallization peak is seen at 116 °C. In contrast, no thermal transitions can be observed within the measured range for TEGPC-4-40%, due to its amorphous structure and the high crosslinking density. This indicates that the integrity of TEGPC-4-40% is maintained, even at temperatures up to 200 °C. This is also higher than common commercial PP and PP/PE/PP separators which have been analysed elsewhere.[50] Previous studies have also shown that, particularly when looking at larger battery packs, the shutdown mechanism in PP/PE/PP separators is insufficient for halting a thermal runaway. Therefore, it is attractive to instead "close the gap" between the separator shrinkage/melting temperature and the battery runaway temperature (typically above 200 °C).[50,51] The close relationship between the separator breakdown temperature and thermal runaway is further described by Feng *et al.*[52] Fig. 6b shows the thermal degradation of the separators using TGA analysis. TEGPC-4-40% has a lower degradation onset point (337 °C) than PE (459 °C), possibly due to the presence of heteroatoms in the polymer structure of TEGPC-4-40%. However, the degradation starts at a temperature that is higher than the battery runaway temperature, and therefore considered sufficiently high.

To gain a better understanding of the mechanical integrity of the separators, dynamic mechanical analysis (DMA) was also performed on the reference PE separator and several formulations of TMs. This is of particular relevance when characterizing highly crosslinked materials, since typically a broad glass

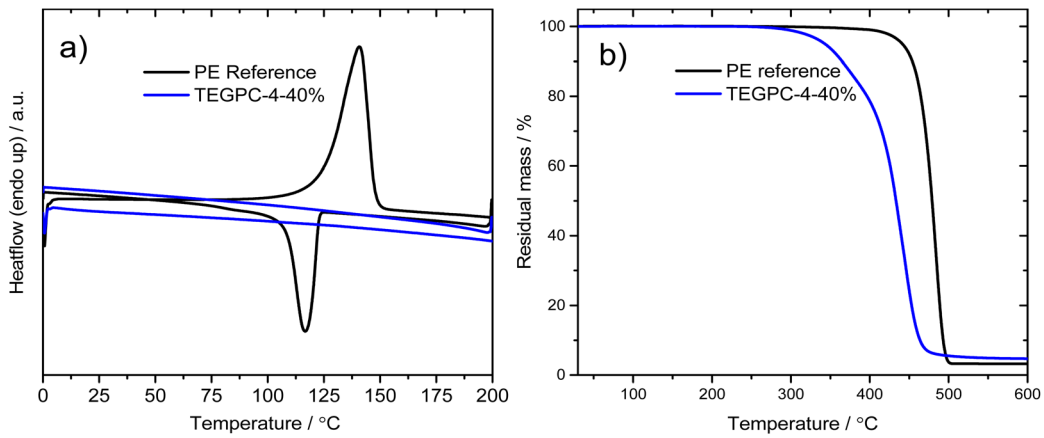


Fig. 6 (a) DSC thermograph with a heating rate of 10 °C $min^{-1}$ and cooling rate of 5 °C $min^{-1}$ and (b) TGA thermograph with a heating rate of 10 °C $min^{-1}$ of a representative thermoset membrane.

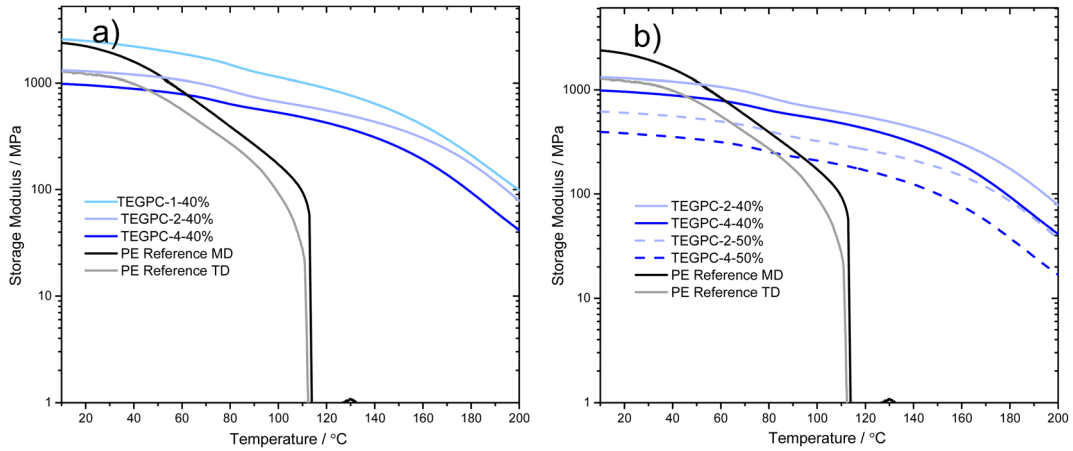


Fig. 7 DMA thermographs for thermoset membranes made with (a) different TEG content and (b) different TEG and total porogen content. The PE reference is added for both the transversal (TD) and machine direction (MD).

transition temperature ($T_g$) is obtained which are difficult to determine using DSC. The storage modulus also gives an indication of the elastic modulus of the material. Fig. 7 shows the PE reference exhibits a relatively high storage modulus at ambient temperatures (above 1000 MPa). This is higher than several other commercial separators that have been tested previously.[53] The separator also exhibits anisotropic properties, with almost double the modulus in one direction. Accurate determination of the modulus of the PE separator proved difficult due to the low thickness (20 μm), with a large spread between samples (see Fig. S6†). In all cases, however, the storage modulus decreases rapidly and a drop-off occurs already at 115 °C, below the melting point of PE. In contrast, all TM formulations exhibit a storage modulus above 100 MPa at 150 °C, which is a good indication of maintained mechanical integrity even at elevated temperatures.

Fig. 7a shows various compositions where the TEG content has been varied, keeping a constant porogen content. In Fig. 7b, the effect of increasing porogen content is instead displayed. In both cases, the curves of the different compositions lie relatively parallel, mainly shifting in storage modulus. This indicates that while the different compositions affect the morphology, the polymer network remains relatively unchanged. A clear correlation between larger pore sizes (in Fig. 4) and a lower storage modulus (or elastic modulus) can also be noted, well in line with previous studies using PIPS.[13,29,34,38] In Table 2, the storage modulus at 25 °C of selected compositions are listed.

### 3.4. Ion transport properties

To study the ion transport properties through the membranes, they were first submerged in liquid electrolyte (LP40) to evaluate their electrolyte uptake. Proper electrolyte uptake is essential for ensuring high and uniform ion transport. The electrolyte uptake is partly due to the affinity of the polymer to the polar solvents in the electrolyte. The presence of polar ethoxylate chains in BPA-DMA are expected to improve the affinity to the electrolyte. However, a high crosslinking density generally restricts solvent absorption, due to the restricted mobility of the polymer chain. More importantly, the porosity plays a crucial role in the electrolyte uptake, as it allows electrolyte to fill the voids in the membranes. Table 2 indeed shows that the formulations made with 40% porogen have a slightly lower electrolyte uptake than the reference. However, when increasing to 50% porogen, an electrolyte uptake above 120% by weight is obtained.

The effective ionic conductivity ($\sigma_{eff}$) of the electrolyte-soaked separators is presented in Table 2. TEGPC-2-40% has a similar $\sigma_{eff}$ to the PE reference, while TEGPC-4-40% displays a doubling in $\sigma_{eff}$. This large increase in $\sigma_{eff}$ is observed despite having a lower electrolyte uptake, suggesting that the pore size and shape lead to lower ionic resistance. TEGPC-2-50% displays the

Table 2 Physical and electrochemical properties of different compositions of TMs and the commercial PE reference

| Sample | Storage modulus/MPa (25 °C) | Electrolyte uptake/% | Ionic conductivity/mS cm$^{-1}$ (25 °C) | $N_M$[a] |
|---|---|---|---|---|
| PE reference | 1095 (TD) | 103 | 0.44 ± 2% | 10.9 |
| TEGPC-2-40% | 1320 | 85 | 0.48 ± 2% | 10.2 |
| TEGPC-4-40% | 943 | 92 | 0.99 ± 4% | 4.9 |
| TEGPC-2-50% | 594 | 128 | 1.4 ± 9% | 3.3 |
| TEGPC-4-40%-10T | 799 | 88 | 0.99 ± 11% | 4.9 |
| TEGPC-2-50%-10T | n.m. | 125 | 1.4 ± 6% | 3.4 |

[a] Calculated based on measured ionic conductivity of liquid electrolyte (EC/DEC 1 M $LiPF_6$) – 4.9 mS cm$^{-1}$.

 

highest $\sigma_{eff}$ at 1.4 mS cm$^{-1}$, which is sufficient for high-power applications. As $\sigma_{eff}$ is highly dependent on the liquid electrolyte conductivity, a more relevant comparison is the MacMullin number, $N_M$, defined as:

$$N_M = \frac{\sigma_{liq}}{\sigma_{eff}} \quad (2)$$

where $\sigma_{liq}$ is the liquid electrolyte conductivity and $\sigma_{eff}$ is the effective conductivity through the separator. With this definition, the lower the $N_M$ is, the less the separator contributes to increasing the ionic resistance. The $N_M$ of the PE reference is around 11, close to previous literature values.[40] TEGPC-4-40% has a $N_M = 4.9$, which is well below the target of $N_M < 8$ set as a general requirement.[3] To validate this value, conductivity measurements were also performed with an alternative liquid electrolyte (EC/PC 1 M LiTFSI), giving the same $N_M$ (see Table S2†). TEGPC-2-50% displays a $N_M$ of 3.3, which is below most commercial battery separators. Landesfeind *et al.*[40] determined the $N_M$ of a large number of separators, where the highly porous Celgard 2500 had an $N_M = 4.5$. These results underline that TMs with high ionic conductivity can be made, and that the TMs can easily be tuned to fit various needs, such as high-power applications where high ionic conductivity is required.

### 3.5. Effect of incorporating thiol monomer

The formulations using purely BPA-DMA as a monomer show promising characteristics, such as high thermomechanical stability and high storage modulus. The compositions with larger pores also display excellent ionic conductivities. However, the formulations with the largest pores (TEGPC-4-40% and TEGPC-2-50%) proved difficult to make thinner than 50 μm, as the films became too brittle. Ideally, the separators should be 25 μm to become competitive with commercial separators.[5] To counteract this issue, the thiol co-monomer tris[(3-mercaptopropionyloxy)-ethyl]-isocyanurate (TEMPIC) was introduced (see Fig. 1). Thiol–ene photopolymerization has become an established alternative to pure (meth)acrylate photopolymerization, exhibiting some key advantages. Firstly, the addition of thiols often leads to faster reaction kinetics. The thiol–ene reaction also occurs *via* step-growth propagation, as opposed to chain-growth, which delays the gel point and generally leads to higher monomer conversion and a more homogeneous polymer network.[54,55] Incorporating a small amount of thiol to methacrylate systems has also been shown to be beneficial in lowering shrinkage stresses during polymerization as well as the thiol-ether linkage increasing network flexibility.[56] Using TEMPIC combines the advantages of thiol–ene reactions while the rigid core ensures that the modulus remains high. Thiol–ene based polymers have also been demonstrated to be chemically stable under the conditions present in lithium-ion batteries.[57–59]

Initial tests were performed by replacing 5, 10 and 20 wt% of BPA-DMA with TEMPIC. A clear increase in monomer conversion was observed with TEGPC-4-40%-10T (containing 10 wt% TEMPIC) exhibiting >90% conversion, compared to 80% for TEGPC-4-40% (see Fig. S4†). Interestingly, despite a partial change in the monomer and polymerization mechanism, no significant changes in morphology could be observed when varying the TEMPIC content (see Fig. S8†). As a consequence, the electrolyte uptake and the ionic conductivity of formulations containing TEMPIC are very similar to the same formulations without TEMPIC (see Table 2). DMA data in Fig. S7† shows a clear decrease in $T_g$ upon increasing TEMPIC content, due to the added flexibility of the thiol-ether linkage. Nevertheless, the sample containing 10 wt% TEMPIC still displays a $T_g = 148$ °C with a storage modulus above 10 MPa at 200 °C, which is expected to be sufficient to maintain dimensional stability. It should also be noted that the tan $\delta$ peak is narrower with the addition of TEMPIC (Fig. S7†), indicating that a more homogenous polymer network is obtained.[54,60] This is expected to have a beneficial effect on the mechanical properties.[61]

For TEGPC-4-40%, the addition of 10 wt% TEMPIC made it less brittle and significantly easier to handle. This is underlined by preliminary uniaxial tensile tests were performed for TEGPC-4-40% and TEGPC-4-40%-10T, shown in Fig. 8. A clear enhancement in the tensile strength and elongation at break can be observed. A rather large spread in elongation at break is observed, which could be expected for thin porous materials where crack initiation points are built into the material. The enhancement of the tensile strength with the addition of TEMPIC is likely due to multiple factors. The flexible thiol-ether linkage and more homogenous polymer network should decrease brittleness. Rather surprisingly, the Young's modulus also increases from 631 ± 45 MPa to 882 ± 21 MPa with the addition of TEMPIC. For this, the pore homogeneity may also play a role, although a deeper analysis of the morphology is needed. Nevertheless, TEGPC-4-40%-10T exhibits excellent mechanical properties, well above commercial requirements.[3] A consequence of the increased tensile strength and toughness for TEGPC-4-40%-10T is also that films could be made which were 20–30 μm thin, making them more commercially viable.

### 3.6. Performance in Li/Li cells

For further electrochemical characterization, TEGPC-4-40% and TEGPC-4-40%-10T were compared to the PE reference. Inspired

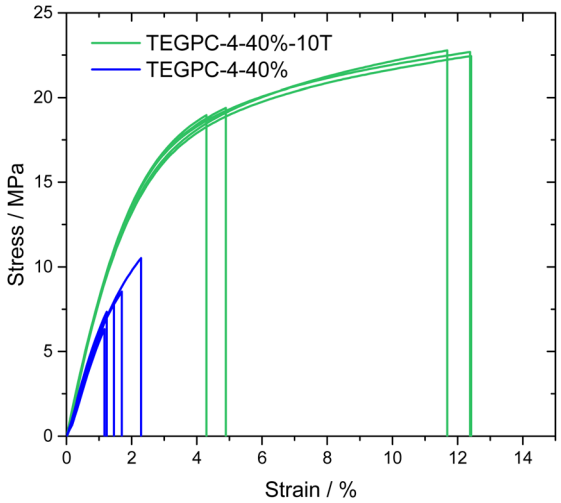


Fig. 8 Stress–strain curves of uniaxial tensile tests for TEGPC-4-40% and TEGPC-4-40%-10T samples.

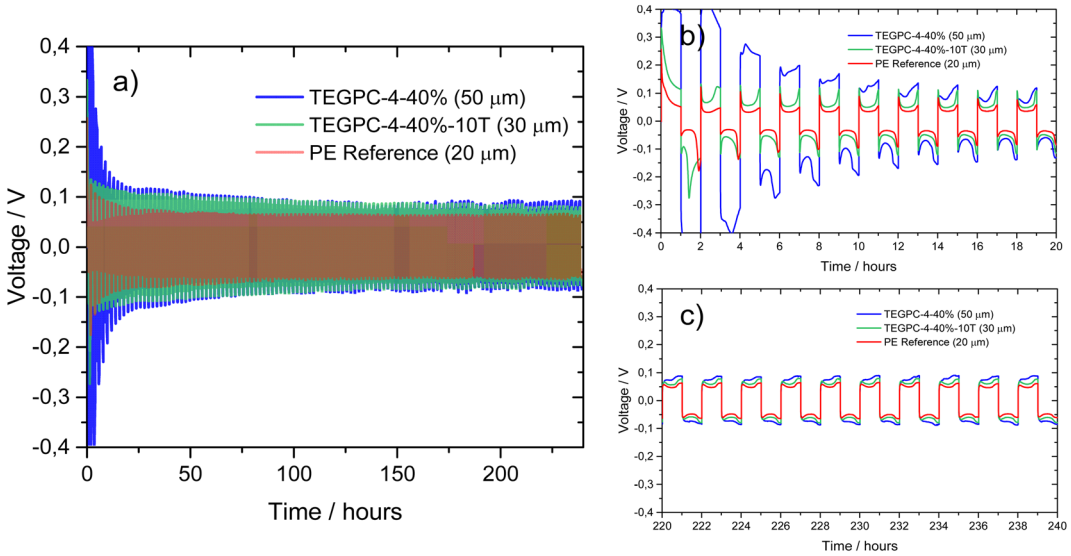


Fig. 9 Voltage profiles of Li/Li symmetrical cell cycling at 0.5 mA $cm^{-1}$ (0.5 mA h $cm^{-1}$) with PE reference and two thermoset membrane formulations for (a) first 240 hours, (b) first 20 hours and (c) hours 220–240. The cells were stopped after 245 hours.

by previous work which have shown that design of separators can improve lithium plating, symmetrical Li/Li cells were constructed to analyse the plating efficiency of the separators.[12,13,62] These tests are also useful to see if the TMs are sufficiently mechanically robust to suppress short circuiting *via* dendrite growth through the separator.

Fig. 9 shows the voltage profiles for Li/Li cells containing either TEGPC-4-40% or TEGPC-4-40%-10T compared to the commercial PE reference. During the first few cycles (Fig. 9b), the initial overpotential is significantly higher for TMs, particularly TEGPC-4-40%, but decreases rapidly before stabilizing after about 10 cycles. This has previously been attributed to SEI formation,[63,64] but could also indicate that there are some residual impurities (moisture, monomer, *etc.*) left in the TMs. The large difference between TEGPC-4-40% and TEGPC-4-40%-10T is rather unexpected, but may be due to a combination of a thicker TM and lower monomer conversion. Such a high initial overpotential could be problematic in full cells, and would require several formation cycles. After stabilizing, all three separators display stable overpotentials with a "peaking" voltage profile which has been suggested to imply that minimal dead lithium is formed.[65] TEGPC-4-40% stills displays the highest overpotential, 63 mV at the middle of the 10$^{th}$ cycle, compared to 48 mV for TEGPC-4-40%-10T and 37 mV for PE reference. The thickness of the respective TMs is one source for the added overpotential, however, given their higher ionic conductivity compared to PE this cannot be the whole explanation. Another source of this overpotential may be the different SEI formations, leading to a higher resistance. Fig. 9c shows that the voltage profiles remain stable over 200 hours, but a slow transfer from a "peaking" voltage profile to a "arching" voltage profile seems to occur, indicating a built-up of dead

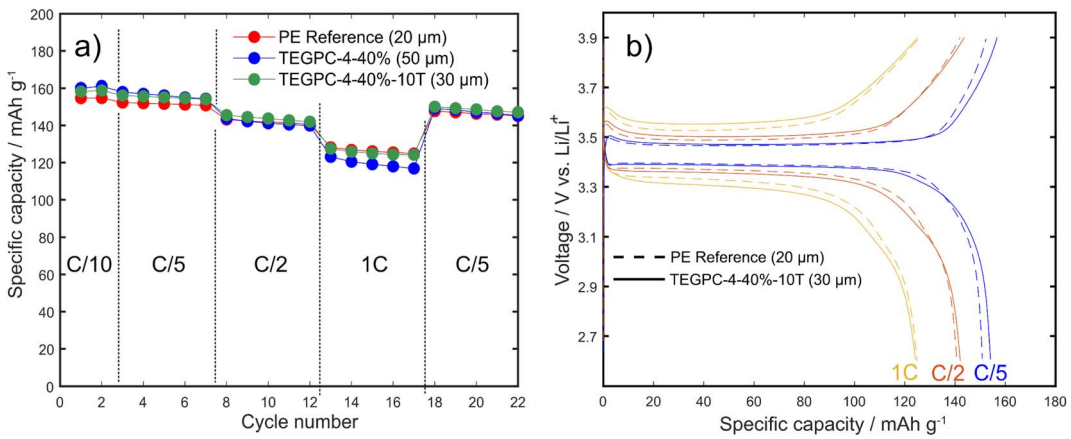


Fig. 10 Cycling performance of LFP/Li half cells cycled from 2.6 to 3.9 V at 22 °C (cathode mass loading = 13.3 mA h $g^{-1}$). (a) Capacity retention test at different C-rates with 1C = 150 mA $g^{-1}$. (b) Voltage *vs.* specific capacity at different C-rates, the final cycle of each step was taken (cycle 7, 12 and 17).

 

lithium.[65] This becomes even more clear in duplicate TEGPC-4-40%-10T and PE reference cells that were cycled for 1600 hours (Fig. S9†). These results indicate that the TM is sufficiently mechanically robust to prevent internal short-circuiting *via* dendrite growth when cycling at the set conditions 0.5 mA $cm^{-1}$, 0.5 mA h $cm^{-1}$ for 1600 hours. However, the plating of lithium ultimately still leads to depletion of the liquid electrolyte and likely growth of mossy lithium, as in the PE reference.[64,65] Increasing the current density further is likely to speed up this process, as shown in previous literature.[65] To summarize, the TMs seem to exhibit a slightly higher overpotential to lithium, however it does not show signs of being more susceptible to short circuiting compared to the PE reference.

### 3.7. Performance in LFP/Li cells

To further test the compatibility of the TMs as separators, half cells were constructed with lithium iron phosphate (LFP) electrodes. Rather often, a low cathode mass loading is used to test of novel electrolyte or separator materials in literature, which can overestimate rate capabilities and cycling stability.[66] The areal capacity of the LFP electrodes used in this study was 2 mA h $cm^{-2}$ (mass loading: 13 mg $cm^{-2}$) which is more commercially relevant. Fig. 10a shows the capacity retention when increasing the current rate from C/10 to 1C. The obtained capacities at low C-rates are similar for both TMs and the PE reference. At 1C, the discharge capacity drops to about 125 mA h $g^{-1}$ for TEGPC-4-40%-10T and the PE reference cells. TEGPC-4-40% shows a slightly lower capacity (115 mA h $g^{-1}$) at 1C, which is likely due to the thickness of the TM. Nevertheless, the TMs manage to maintain a reasonable capacity at 1C and a 2 mA h $cm^{-2}$, which corresponds to the rather high lithium plating current rate of 2 mA $cm^{-2}$.

Throughout the capacity retention test, the difference between the PE reference and TEGPC-4-40%-10T are marginal as demonstrated by the voltage profiles at different C-rates seen in Fig. 10b. Fig. S10† also shows duplicate cells that were constructed at another time point. The batch-to-batch difference is larger than the difference between the different membranes, indicating that particularly TEGPC-4-40%-10T is on par with the reference material. Finally, when returning to a lower C-rate (C/5), the capacity returns to 150 mA h $g^{-1}$ which indicates that no significant irreversible capacity loss occurred during faster charging. The low initial capacity of some of the TMs in Fig. S10† indicates that the TMs are more sensitive to small variations in the preparation conditions.

TEGPC-4-40%-10T and the reference were also used in an LFP/Li half-cell that was cycled at C/5 for 50 cycles. Fig. 11 shows the discharge capacity as a function of cycle number. The cells showed similar initial capacity (150–155 mA h $g^{-1}$), decreasing steadily to 125–130 mA h $g^{-1}$ over 50 cycles. The capacity retention was similar, around 83% for TEGPC-4-40%-10T and 84% for the reference. Fig. 11 also shows that the coulombic efficiency (CE) for most cycles is around 98%, which is rather low, but not uncommon when using lithium metal as a counter electrode.[67] This is likely mainly due to degradation of the liquid electrolyte and non-optimized experimental conditions (no additives used, CC/CC charging, *etc.*). Although similar, the CE is slightly lower for TEGPC-4-40%-10T, which could indicate some instabilities in this membrane. Since the difference is so marginal, this is more likely due to residual contaminants from the fabrication process. Further investigation into the long-term stability is the subject of future work.

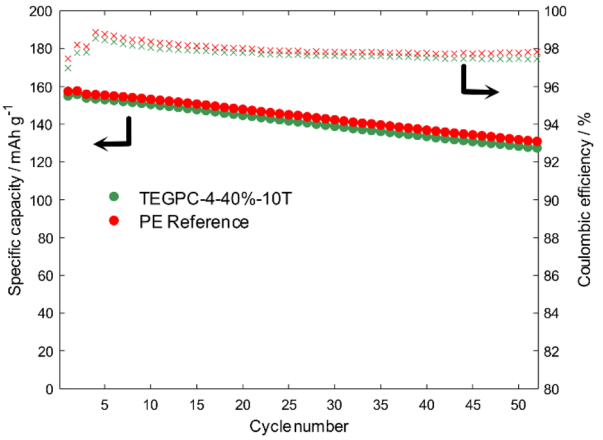


Fig. 11 Cycling performance of LFP/Li half cells using a TEGPC-4-40%-10T separator (green) or PE reference (red), cycled from 2.6 to 3.9 V at 22 °C. Two formation cycles at C/10 were followed by 50 cycles at C/5.

## 4. Conclusions

In the present study, the use of photopolymerization-induced phase separation as a scalable process to produce methacrylate-based thermoset membranes is investigated. A combination of PC and TEG as safe and cheap porogens are used. When increasing the TEG content and the total porogen content, the pore size increases. By tuning the ratio between PC and TEG, different morphologies are achieved. Due to the high crosslinking density of the methacrylate thermoset, the membranes display high thermomechanical properties. The membranes maintain dimensional stability above 200 °C, well above the temperature at which the commercial PE reference starts to melt. The study also shows that the elastic modulus of the membranes clearly decreases with increasing pore size and the formulations with the highest pore size become brittle, making it difficult to make thin films (<50 μm). To counteract this problem, a small amount of a thiol monomer (TEMPIC) was added which significantly increases the toughness of the material and made it possible to produce thinner membranes. An improvement of the Young's modulus is also achieved (880 MPa), above the industry requirement. The ionic conductivities of the different membrane formulations were similar or better than the commercial reference, with TEGPC-4-40%-10T displaying a conductivity of 1 mS $cm^{-2}$ and a $N_M = 4.9$. Selected membranes were tested in Li/Li symmetrical cells, showing sufficient mechanical stability to avoid short circuits. A slow overpotential build up due to electrolyte depletion was seen, similar to the PE reference. LFP half cells with an areal capacity of 2 mA h $cm^{-2}$ were cycled at different C-rates, with TEGPC-4-

40%-10T displaying a similar performance to the PE reference. In summary, this study contributes to further development of thermoset membranes as battery separators by presenting a scalable and efficient way to manufacture membranes using photopolymerization-induced phase separation in ambient conditions.

## Data availability

The data supporting this article have been included as part of the ESI.†

## Author contributions

Conceptualization, S. E., M. J., investigation, S. E., funding acquisition, M. J., G. L. The manuscript was written through contributions of all authors. All authors have given approval to the final version of the manuscript.

## Conflicts of interest

There are no conflicts to declare.

## Acknowledgements

The authors would like to acknowledge financial support from BASE Battery Sweden (Vinnova grant: 2019-00064). The research group Kombatt and colleagues at the Division of Electrochemistry at KTH are acknowledged for helpful discussions.

## References

1 A. A. Tidblad, K. Edström, G. Hernández, I. de Meatza, I. Landa-Medrano, J. Jacas Biendicho, L. Trilla, M. Buysse, M. Ierides, B. P. Horno, Y. Kotak, H.-G. Schweiger, D. Koch and B. S. Kotak, *Energies*, 2021, **14**, 4223.
2 M. F. Lagadec, R. Zahn and V. Wood, *Nat. Energy*, 2018, **4**, 16–25.
3 P. Arora and Z. Zhang, *Chem. Rev.*, 2004, **104**, 4419–4462.
4 F. Wang, X. Ke, K. Shen, L. Zhu and C. Yuan, *Adv. Mater. Technol.*, 2022, **7**, 2100772.
5 N. Lingappan, W. Lee, S. Passerini and M. Pecht, *Renewable Sustainable Energy Rev.*, 2023, **187**, 113726.
6 X. Huang, *J. Solid State Electrochem.*, 2011, **15**, 649–662.
7 C. Shi, P. Zhang, L. Chen, P. Yang and J. Zhao, *J. Power Sources*, 2014, **270**, 547–553.
8 J. Moon, J. Y. Jeong, J. I. Kim, S. Kim and J. H. Park, *J. Power Sources*, 2019, **416**, 89–94.
9 K. J. Kim, Y. H. Kim, J. H. Song, Y. N. Jo, J.-S. Kim and Y.-J. Kim, *J. Power Sources*, 2010, **195**, 6075–6080.
10 H. Chen, Z. Wang, Y. Feng, S. Cai, H. Gao, Z. Wei and Y. Zhao, *Chem. Eng. J.*, 2023, **471**, 144593.
11 Y. Pan, S. Chou, H. K. Liu and S. X. Dou, *Natl. Sci. Rev.*, 2017, **4**, 917–933.
12 R. Pan, R. Sun, Z. Wang, J. Lindh, K. Edström, M. Strømme and L. Nyholm, *Nano Energy*, 2019, **55**, 316–326.
13 M. Li, H. Li, J.-L. Lan, Y. Yu, Z. Du and X. Yang, *J. Mater. Chem. A*, 2018, **6**, 19094–19106.
14 Y. H. Chen, P. Lennartz, K. L. Liu, Y. C. Hsieh, F. Scharf, R. Guerdelli, A. Buchheit, M. Grünebaum, F. Kempe, M. Winter and G. Brunklaus, *Adv. Funct. Mater.*, 2023, **33**, 2300501.
15 C. Fu, G. Homann, R. Grissa, D. Rentsch, W. Zhao, T. Gouveia, A. Falgayrat, R. Lin, S. Fantini and C. Battaglia, *Adv. Energy Mater.*, 2022, **12**, 2200412.
16 Q. Liang, L. Chen, J. Tang, X. Liu, J. Liu, M. Tang and Z. Wang, *Energy Storage Mater.*, 2023, **55**, 847–856.
17 J. Wan, J. Xie, X. Kong, Z. Liu, K. Liu, F. Shi, A. Pei, H. Chen, W. Chen, J. Chen, X. Zhang, L. Zong, J. Wang, L.-Q. Chen, J. Qin and Y. Cui, *Nat. Nanotechnol.*, 2019, **14**, 705–711.
18 V. Deimede and C. Elmasides, *Energy Technol.*, 2015, **3**, 453–468.
19 H. Heimes, A. Kampker, C. Offermanns, N. Lackner, T. Elliger, V. Mussehl, S. Michaelis and J. Zienow, *Production of Lithium-Ion Battery Cell Components*, 2nd edn, 2023.
20 F. Svec, *J. Chromatogr. A*, 2010, **1217**, 902–924.
21 C. Viklund, F. Svec, J. M. J. Fréchet and K. Irgum, *Chem. Mater.*, 1996, **8**, 744–750.
22 F. Svec and J. M. J. Frechet, *Anal. Chem.*, 1992, **64**, 820–822.
23 N. Tsujioka, N. Ishizuka, N. Tanaka, T. Kubo and K. Hosoya, *J. Polym. Sci., Part A: Polym. Chem.*, 2008, **46**, 3272–3281.
24 K. Nakanishi and N. Tanaka, *Acc. Chem. Res.*, 2007, **40**, 863–873.
25 J. P. Pascault and R. J. J. Williams, *Overview of thermosets: present and future*, Elsevier, 2018, pp. 3–34, DOI: 10.1016/b978-0-08-101021-1.00001-0.
26 M. W. Schulze, L. D. McIntosh, M. A. Hillmyer and T. P. Lodge, *Nano Lett.*, 2014, **14**, 122–126.
27 L. E. Asp, M. Johansson, G. Lindbergh, J. Xu and D. Zenkert, *Funct. Compos. Struct.*, 2019, **1**, 042001.
28 M. Y. Tan, D. Safanama, S. S. Goh, J. Y. C. Lim, C. H. Lee, J. C. C. Yeo, W. Thitsartarn, M. Srinivasan and D. W. H. Fam, *Chem.–Asian J.*, 2022, **17**, e202200784.
29 N. Shirshova, A. Bismarck, E. S. Greenhalgh, P. Johansson, G. Kalinka, M. J. Marczewski, M. S. P. Shaffer and M. Wienrich, *J. Phys. Chem. C*, 2014, **118**, 28377–28387.
30 N. Shirshova, A. Bismarck, S. Carreyette, Q. P. V. Fontana, E. S. Greenhalgh, P. Jacobsson, P. Johansson, M. J. Marczewski, G. Kalinka, A. R. J. Kucernak, J. Scheers, M. S. P. Shaffer, J. H. G. Steinke and M. Wienrich, *J. Mater. Chem. A*, 2013, **1**, 15300.
31 N. Ihrner, W. Johannisson, F. Sieland, D. Zenkert and M. Johansson, *J. Mater. Chem. A*, 2017, **5**, 25652–25659.
32 L. M. Schneider, N. Ihrner, D. Zenkert and M. Johansson, *ACS Appl. Energy Mater.*, 2019, **2**, 4362–4369.
33 W. Johannisson, N. Ihrner, D. Zenkert, M. Johansson, D. Carlstedt, L. E. Asp and F. Sieland, *Compos. Sci. Technol.*, 2018, **168**, 81–87.
34 S. Emilsson, V. Vijayakumar, J. Mindemark and M. Johansson, *Electrochim. Acta*, 2023, **449**, 142176.
35 M. Cattaruzza, Y. Fang, I. Furó, G. Lindbergh, F. Liu and M. Johansson, *J. Mater. Chem. A*, 2023, **11**, 7006–7015.

 

36 S. Duan, M. Cattaruzza, V. Tu, R. M. Auenhammer, R. Jänicke, M. K. G. Johansson, F. Liu and L. E. Asp, *Commun. Mater.*, 2023, **4**, 49.
37 K. Sakakibara, H. Kagata, N. Ishizuka, T. Sato and Y. Tsujii, *J. Mater. Chem. A*, 2017, **5**, 6866–6873.
38 A. J. Manly and W. E. Tenhaeff, *J. Mater. Chem. A*, 2022, **10**, 10557–10568.
39 A. J. Manly and W. E. Tenhaeff, *Electrochim. Acta*, 2022, **425**, 140705.
40 J. Landesfeind, J. Hattendorff, A. Ehrl, W. A. Wall and H. A. Gasteiger, *J. Electrochem. Soc.*, 2016, **163**, A1373–A1387.
41 D. W. Van Krevelen and K. Te Nijenhuis, in *Properties of Polymers*, ed. D. W. Van Krevelen and K. Te Nijenhuis, Elsevier, Amsterdam, 4th edn, 2009, pp. 129–188, DOI: 10.1016/B978-0-08-054819-7.00006-6.
42 B. Schäffner, F. Schäffner, S. P. Verevkin and A. Börner, *Chem. Rev.*, 2010, **110**, 4554–4581.
43 J. Fowles, M. Banton, J. Klapacz and H. Shen, *Toxicol. Lett.*, 2017, **278**, 66–83.
44 M. D. Soucek and X. Ren, in *Photocured Materials*, ed. A. Tiwari and A. Polykarpov, The Royal Society of Chemistry, 2014, DOI: 10.1039/9781782620075-00015.
45 H. Yoshihara and M. Yamamura, *J. Appl. Polym. Sci.*, 2019, **136**, 47867.
46 W. D. Cook, *Polymer*, 1992, **33**, 2152–2161.
47 J. W. Stansbury, *Dent. Mater.*, 2012, **28**, 13–22.
48 M. H. Mohamed and L. D. Wilson, *Nanomaterials*, 2012, **2**, 163–186.
49 H. M. J. Boots, J. G. Kloosterboer, C. Serbutoviez and F. J. Touwslager, *Macromolecules*, 1996, **29**, 7683–7689.
50 C. J. Orendorff, T. N. Lambert, C. A. Chavez, M. Bencomo and K. R. Fenton, *Adv. Energy Mater.*, 2013, **3**, 314–320.
51 E. P. Roth, D. H. Doughty and D. L. Pile, *J. Power Sources*, 2007, **174**, 579–583.
52 X. Feng, X. He, M. Ouyang, L. Wang, L. Lu, D. Ren and S. Santhanagopalan, *J. Electrochem. Soc.*, 2018, **165**, A3748.
53 C. T. Love, *J. Power Sources*, 2011, **196**, 2905–2912.
54 C. E. Hoyle and C. N. Bowman, *Angew. Chem., Int. Ed.*, 2010, **49**, 1540–1573.
55 T. Y. Lee, Z. Smith, S. K. Reddy, N. B. Cramer and C. N. Bowman, *Macromolecules*, 2007, **40**, 1466–1472.
56 H. Lu, J. A. Carioscia, J. W. Stansbury and C. N. Bowman, *Dent. Mater.*, 2005, **21**, 1129–1136.
57 C. Zuo, B. Zhou, Y. H. Jo, S. Li, G. Chen, S. Li, W. Luo, D. He, X. Zhou and Z. Xue, *Polym. Chem.*, 2020, **11**, 2732–2739.
58 S. Park, B. Jeong, D.-A. Lim, C. H. Lee, K. H. Ahn, J. H. Lee and D.-W. Kim, *ACS Appl. Mater. Interfaces*, 2020, **12**, 19553–19562.
59 J. Hu, W. Wang, B. Zhou, J. Sun, W. S. Chin and L. Lu, *Small*, 2024, **20**, 2306622.
60 B. H. Jones, T. M. Alam, S. Lee, M. C. Celina, J. P. Allers, S. Park, L. Chen, E. J. Martinez and J. L. Unangst, *Polymer*, 2020, **205**, 122783.
61 A. Shundo, M. Aoki, P. Wang, T. Hoshino, S. Yamamoto, S. Yamada and K. Tanaka, *Macromolecules*, 2023, **56**, 3884–3890.
62 R. Pan, R. Sun, Z. Wang, J. Lindh, K. Edström, M. Strømme and L. Nyholm, *Energy Storage Mater.*, 2019, **21**, 464–473.
63 G. Bieker, M. Winter and P. Bieker, *Phys. Chem. Chem. Phys.*, 2015, **17**, 8670–8679.
64 B. Wu, J. Lochala, T. Taverne and J. Xiao, *Nano Energy*, 2017, **40**, 34–41.
65 K.-H. Chen, K. N. Wood, E. Kazyak, W. S. Lepage, A. L. Davis, A. J. Sanchez and N. P. Dasgupta, *J. Mater. Chem. A*, 2017, **5**, 11671–11681.
66 P. Lennartz, B. A. Paren, A. Herzog-Arbeitman, X. C. Chen, J. A. Johnson, M. Winter, Y. Shao-Horn and G. Brunklaus, *Joule*, 2023, **7**, 1471–1495.
67 G. M. Hobold, J. Lopez, R. Guo, N. Minafra, A. Banerjee, Y. Shirley Meng, Y. Shao-Horn and B. M. Gallant, *Nat. Energy*, 2021, **6**, 951–960.